



An all-diamond X-ray position and flux monitor using nitrogen-incorporated ultra-nanocrystalline diamond contacts

Mengnan Zou,^a Mengjia Gaowei,^b Tianyi Zhou,^a Anirudha V. Sumant,^c Chernojaye,^e Daniel A. Fisher,^e Jen Bohon,^d John Smedley^b and Erik M. Muller^{a*}

Received 1 February 2018

Accepted 24 April 2018

Edited by P. A. Pianetta, SLAC National Accelerator Laboratory, USA

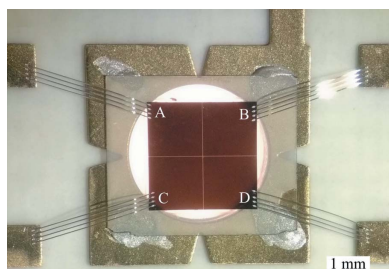
Keywords: X-ray detector; beam position monitor; diamond; ultra-nanocrystalline; flux monitor.

^aMaterials Science and Chemical Engineering, Stony Brook University, Stony Brook, NY 11794, USA, ^bInstrumentation Division, Brookhaven National Laboratory, Upton, NY 11973, USA, ^cCenter for Nanoscale Materials, Argonne National Laboratory, Argonne, IL 60439, USA, ^dCenter for Synchrotron Biosciences, Department of Nutrition, Case Western Reserve University, Cleveland, OH 44106, USA, and ^eNational Institute of Standards and Technology, Gaithersburg, MD 20899, USA. *Correspondence e-mail: erik.muller@stonybrook.edu

Diamond X-ray detectors with conducting nitrogen-incorporated ultra-nanocrystalline diamond (N-UNCD) films as electrodes were fabricated to measure X-ray beam flux and position. Structural characterization and functionality tests were performed for these devices. The N-UNCD films grown on unseeded diamond substrates were compared with N-UNCD films grown on a seeded silicon substrate. The feasibility of the N-UNCD films acting as electrodes for X-ray detectors was confirmed by the stable performance in a monochromatic X-ray beam. The fabrication process is able to change the surface status which may influence the signal uniformity under low bias, but this effect can be neglected under full collection bias.

1. Introduction

The extraordinary properties of diamond, such as radiation hardness, thermal conductivity and indirect band-gap, make it an ideal material for synchrotron X-ray radiation detectors (Bergonzo *et al.*, 1999). In the past, diamond X-ray detectors have often been fabricated with metal contacts like platinum, providing absolute flux calibration and position resolution better than 50 nm (Zhou *et al.*, 2015). For many applications, diamond detectors with metal contacts have proven very reliable, and several commercial options are now available, including a variety of detector configurations from Sydor Instruments LLC and Cividec Instrumentation. However, for many energy-scanning applications, the absorption edges from the metallic contacts alter the X-ray spectrum, affecting downstream experiments. Ravel *et al.* (2013) displayed the X-ray absorption spectroscopy-like scan over a broad range of energy and the absorption edge measured for Co foil is clearly visible. Platinum, aluminium and titanium are common metals used for contacts on diamond radiation detectors; however, the presence of absorption edges in both the soft and hard X-ray ranges limits the available range for energy-scanning experiments. Also, many metals are incompatible with biological organisms, thus limiting the application of diamond detectors as biomedical devices. Although diamond itself performs remarkably well in high-flux environments, the contacts and surrounding material may suffer damage. For example, carbon buildup on the contact surface from X-ray radiation of low concentrations of residual gases in a vacuum



© 2018 International Union of Crystallography

system can result in electrical shorts between contacts, which was observed in the white-beam diamond detectors installed just after the undulator at the X25 beamline, National Synchrotron Light Source (NSLS), USA (Muller *et al.*, 2012). Additionally, excessive heating of the detector due to absorbed X-ray power or ohmic heating can compromise the oxygen termination on the interface of the diamond and the contacts. Consequently, replacement of metal contacts is highly desirable. Recent advances include the development of carbon-based contacts, such as diamond-like carbon (Desjardins *et al.*, 2018) and laser graphitization of contacts from the diamond surface (Feudis *et al.*, 2017). Extending this effort, nitrogen-incorporated ultra-nanocrystalline diamond (N-UNCD) is presented as an ideal contact material, with no additional absorption edges, excellent biocompatibility (Narayan, 2013) and many of the other benefits of diamond.

In this paper, the fabrication, characterization and calibration of diamond X-ray detectors with N-UNCD contacts (referred to as the 'UNCD detector') will be discussed. Several UNCD detectors have been fabricated and tested at multiple beamlines across a variety of energy ranges. X-ray beam flux calibration, beam position calibration and X-ray beam-induced current (XBIC) mapping were carried out at the G2 beamline (Cornell High Energy Synchrotron Source, CHESS, USA), and at the X-ray Footprinting beamline (XFP, NSLS-II, USA). Characterization of the UNCD contact layers was studied by Raman spectroscopy and scanning electron microscopy (SEM) to confirm the grain structure of the N-UNCD film. In addition, near-edge X-ray absorption fine-structure measurements across the carbon *K*-edge were carried out at the U7A beamline (NEXAFS, NSLS) to determine the carbon bonding environment. In all cases, the UNCD detectors performed well, verifying UNCD as a superior alternative material for contacts on diamond radiation monitors.

2. Experimental

Several electronic-grade (nitrogen impurity concentration <1 part per billion) single-crystal diamonds grown by chemical vapor deposition (CVD) from IIA Technologies, Pte Ltd and Element Six were used for the detector fabrication. Typical diamond sizes were 4 mm × 4 mm × 100 μm, polished to a surface roughness better than 5 nm r.m.s. Prior to fabrication, the diamonds were screened using birefringence imaging to evaluate crystal quality. Previous reports on diamond detector performance indicate that the high strain fields from inclusions generate regions of increased detector response where the detector current is no longer linear in absorbed X-ray power due to hole injection (Muller *et al.*, 2009) and that some defects reduce carrier mobility (Lohstroh *et al.*, 2007); these effects would impact the evaluation of the N-UNCD contact performance. Three diamonds with high quality and low defect density were selected for UNCD detector fabrication, with clean birefringence images in the active areas.

2.1. N-UNCD growth

Diamond substrates were cleaned chemically prior to crystal growth, but no seeding process was conducted. N-UNCD films were grown on both sides of the diamonds using a 950 MHz microwave plasma chemical vapor deposition (MPCVD) system at the Center for Nanoscale Materials, Argonne National Laboratory. A mixture of Ar (180 sccm) (sccm = standard cubic centimeters per minute), H₂ (18 sccm) and CH₄ (2 sccm) at a pressure of 100 Torr was employed during the deposition while the substrate temperature and the input microwave power were kept at 800°C and 950 W, respectively. Three diamonds were coated with UNCD over their entire surface at a rate of 250 nm h⁻¹ and are referred to as UNCD I, UNCD II and UNCD III. They have thicknesses of 400 nm, 700 nm and 100 nm, respectively. UNCD III has an additional 100 nm-thick intrinsic UNCD layer deposited on top of an already patterned N-UNCD layer as a protective overlayer.

2.2. Fabrication process and assembly

The diamond samples with N-UNCD films covering the entire surface were gently cleaned successively by acetone, isopropyl alcohol and deionized water. The samples were then patterned by 1 μm-thick nickel (Ni) films to protect the areas where the UNCD films would act as contacts. The Ni masks were patterned by a standard photolithography process. The N-UNCD films in the areas not protected by the Ni masks were then removed thoroughly by reactive ion etching (RIE) using O₂/CHF₃ plasma at -20°C and with 2000 W ICP power. The RIE time was estimated from the thickness of N-UNCD film (etching rate is ~150 nm min⁻¹) and a global over-etch (200–300 nm) was performed to ensure no N-UNCD remained. After the etching process, the Ni mask was removed using dilute nitric acid, leaving the N-UNCD underneath as contacts for the UNCD detectors.

UNCD I was patterned as a quadrant UNCD detector, with on one side a single 2.5 mm × 2.5 mm square and on the other side a 2.5 mm square with 20 μm-wide electrode gap, as shown in Fig. 1(a). UNCD II was patterned as a 16 virtual pixel UNCD detector, with both sides consisting of four 700 μm-wide stripes with 50 μm-wide streets (with the pattern rotated by 90° on the second side to form 'pixels'), as shown in Fig. 1(b). These two detectors were prepared for detector performance testing. Another two UNCD detectors were fabricated to address potential problems for practical application. Specifically, UNCD III was patterned twice; first, UNCD III(a) was tested as a single-channel UNCD detector, with both sides patterned with a 3 mm-diameter disk; once tested, UNCD III(b) was cleaned and repatterned to be a quadrant UNCD detector, with 40 μm-wide cross streets on one side. A non-conductive intrinsic diamond layer was deposited over the entire diamond as protection from potential shorting due to subsequent carbon buildup from prolonged exposure to high-flux X-rays, see Fig. 1(c).

After the fabrication process, the diamonds were adhered to circuit boards with silver paint, which provided electrical

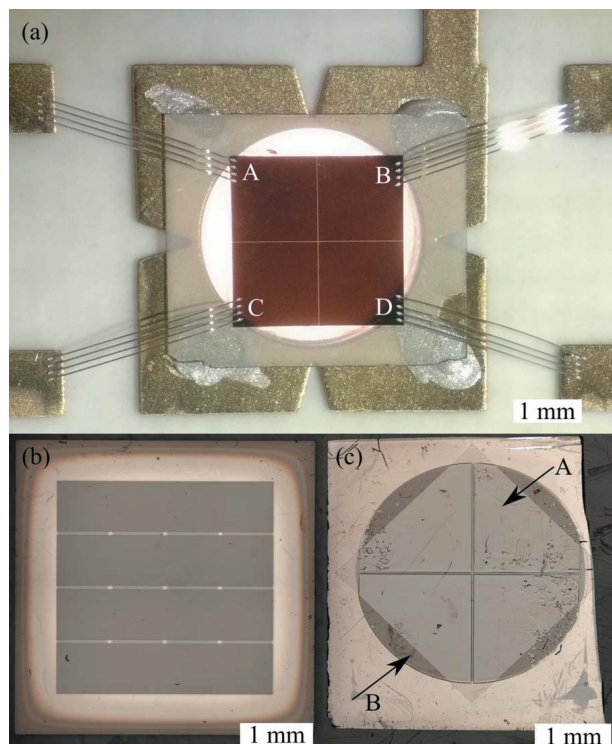


Figure 1 (a) The UNCD I detector. (b) The UNCD II detector. (c) The UNCD III detector. The area indicated by the arrow A is the intrinsic polycrystalline diamond layer. Arrow B indicates the N-UNCD contacts.

contact to the single-pad contact. The quadrant sides were wire-bonded to the pre-designed circuit boards with 25 μm -thick aluminium wires (3% Si) directly to the N-UNCD contacts, shown in Fig. 1(a). Four wire-bonds were used on each of the quadrant contacts for redundancy and to increase current capacity.

2.3. Experimental setup for diamond detector calibration

The N-UNCD detectors were tested at the G2 beamline at CHESS using a monochromatic X-ray beam with a photon energy of 11.32 keV. The experimental setup is illustrated in Fig. 2. The beam size was defined by slits (part A) and the incident flux was monitored by a 6 cm-long nitrogen-filled

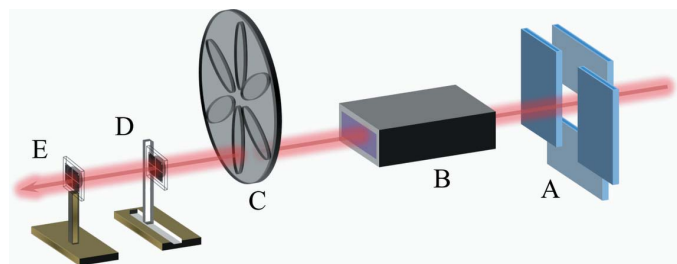


Figure 2 Schematic of the experimental setup at G2, CHESS (A: slits for beam size definition; B: ion chamber with N_2 gas; C: aluminium attenuator; D: UNCD detector on the micro-motor; E: static reference detector).

ionization chamber (part B). Different thicknesses of aluminium attenuators (part C) were used to control the incident flux. Two diamond detectors were aligned downstream with the quadrant sides facing the incident X-ray beam. The UNCD detector (part D) was mounted on a high-resolution x - y translation stage with motion perpendicular to the incident beam. Behind the UNCD detector, a previously calibrated diamond detector with Pt contacts (part E) was fixed in place as a transmission monitor. A similar setup was used at the XFP beamline for higher flux calibration in white beam (5–20 keV), using pinholes instead of slits. Each of the N-UNCD detectors was tested using this experimental setup.

3. Results and discussion

3.1. UNCD structural characterization by Raman spectroscopy and NEXAFS

It is standard practice in UNCD growth to first seed a substrate; as no seeding process was performed before the N-UNCD film growth on these UNCD devices, the Raman spectra between a known UNCD sample and the UNCD grown for our detectors was measured. Three samples were tested, a 400 nm-thick N-UNCD film on a seeded silicon substrate (control sample, indicated as #0), a 400 nm-thick N-UNCD film on the unseeded diamond substrate (from UNCD I, indicated as #1) and a 700 nm-thick N-UNCD film on an unseeded diamond substrate (from UNCD II, indicated as #2), using confocal Raman spectroscopy with a 532 nm laser. Several areas were measured on each sample, displaying the uniformity of the N-UNCD film growth. As shown in Fig. 3, all three spectra display the typical shape of the Raman spectrum from an N-UNCD film (Garrett *et al.*, 2012), with two trans-polyacetylene (t-PA) peaks near 1150 cm^{-1} and 1480 cm^{-1} . The t-PA peaks represent the existence of a type

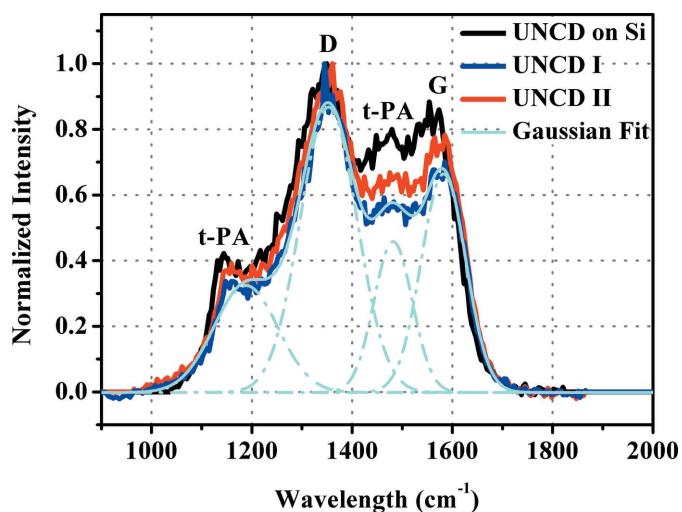


Figure 3 Raman spectra excited by a 532 nm laser from the N-UNCD film grown on the seeded Si substrate (400 nm-thick), UNCD I (400 nm-thick N-UNCD film grown on the unseeded diamond substrate) and UNCD II (700 nm-thick N-UNCD film grown on the unseeded diamond substrate).

of sp^2 carbon atom bonded with a single hydrogen atom. This type of carbon atom is predominately distributed on the grain boundaries and on the surface, and is ascribed to the nanoscale crystallinity of the diamond (Gruen, 1999). Considering that the two t-PA peaks always appear together with similar dispersions (Kuzmany *et al.*, 2004), we use the first t-PA peak for the following analysis. Two other broad peaks, the D peak near 1350 cm^{-1} and the G peak near 1580 cm^{-1} , reveal that the film is composed of both sp^3 and sp^2 carbon atoms (Arenal *et al.*, 2007). The nitrogen incorporation level was similar for all samples, estimated as 20% according to the N_2 additive in the growth recipe in §2.1.

Fitting each peak to a Gaussian shape, the peaks with high consonance to experimental data are resolved and the peak positions and corresponding normalized intensity are included in Table 1. All the characteristic peak positions from the spectra of both N-UNCD films on the diamond substrates (#1 and #2) are blue-shifted compared with those from the N-UNCD film on the silicon substrate (#0), representing a decrease in the sp^2 carbon fraction in the N-UNCD films on the unseeded diamond substrates. Despite the blue-shift tendency, the relative positions between each characteristic peak remains consistent, illustrating the similar nitrogen incorporation level in the three samples regardless of the substrate material (Yuan *et al.*, 2016).

The intensity of each characteristic peak is indicated as I_D for the D peak, I_G for the G peak and I_T for the first t-PA peak, indicative of disordered sp^2 carbon and differently bonded sp^2 carbons, respectively. The intensity ratios I_T/I_G and I_D/I_G can be calculated to analyze the carbon phases in the N-UNCD films. Compared with #0, #1, which shares a similar thickness of N-UNCD film, has higher values for both I_T/I_G and I_D/I_G . The value of I_T/I_G increases with the rising density of the sp^2 carbon atoms distributed along the grain boundaries, while the value of I_D/I_G increases with rising ratio between sp^3 and sp^2 carbon atoms. Thus the N-UNCD film grown on the unseeded diamond substrate has a higher proportion of sp^2 carbon atoms aggregated along the grain boundaries compared with the N-UNCD film grown on the seeded Si substrate, although the total proportion of sp^2 carbon atoms is lower. This phenomenon becomes more noticeable as the UNCD films become thicker (#2), which may be related to the nucleation and growth mechanism on different substrate materials.

As for results from the N-UNCD films on the diamond substrates (#1 and #2), the intensity ratios I_T/I_G and I_D/I_G both increase as the N-UNCD film thickness grows, indicating an increase in sp^2 carbon atoms aggregated along the grain boundaries but a reduction in proportion of sp^2 carbon atoms. This implies that the grain size increases and the grain boundary areas decrease with the N-UNCD film growth on the diamond substrate.

NEXAFS measurements were conducted at the NIST beamline U7A of NSLS. A soft X-ray beam of diameter 0.75 mm was used to excite photoemission from the sample

Table 1

Peak positions and normalized intensity for Raman spectra from samples.

Peak Sample	t-PA			D			G		
	#1	#2	#3	#1	#2	#3	#1	#2	#3
Position (cm^{-1})	1159	1180	1188	1343	1353	1353	1563	1580	1582
Normalized intensity	0.36	0.35	0.33	0.93	0.93	0.87	0.83	0.75	0.67

surface and simultaneously generate charge carriers in the device. NEXAFS spectra were collected in partial electron yield (PEY) mode with a retarding bias of 50 V, which in this measurement corresponds to a probing depth of 50 nm. X-ray induced current was collected simultaneously through a Keithly 6517 electrometer. A photon energy range of 260 eV to 330 eV was used to study the carbon K -edge features around 284 eV and all collected spectra were normalized by the current measured in a clean gold mesh and energy calibrated by a carbon mesh. Post-data analysis was accomplished using the software *ATHENA* and *Igor*.

Fig. 4 shows the NEXAFS spectra from the N-UNCD thin film. The spectra taken from HOPG (highly oriented pyrolytic graphite) and a clean electronic grade CVD single-crystal diamond are shown for comparison. All spectra were pre- and post-edge normalized using *ATHENA* (Ravel & Newville, 2005). From the comparison it can be observed that the N-UNCD NEXAFS spectrum contains distinct features from both diamond and graphite, labeled (a)–(d). Feature (a) is the carbon $1s-\pi^*$ resonance at 285.5 eV observed in both N-UNCD and HOPG spectra. The sharp rise at 289.5 eV,

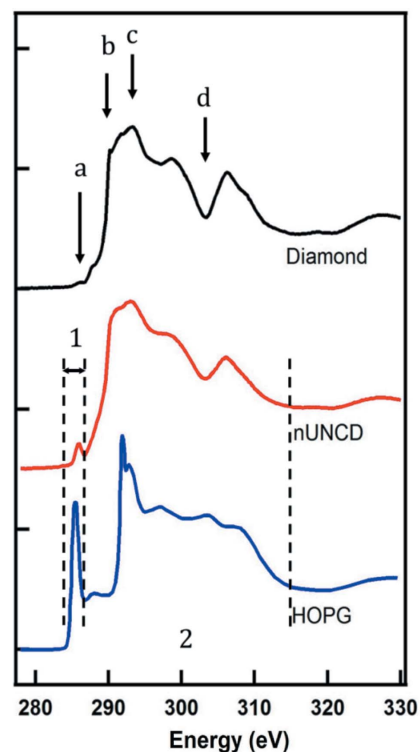


Figure 4 Normalized carbon K -edge NEXAFS PEY spectra for a clean CVD diamond, diamond detector with N-UNCD contact, and an HOPG reference.

labeled feature (b), is due to the first diamond excitation. Feature (c) is the diamond $1s-\sigma^*$ resonance, while the second diamond band gap is labeled feature (d). Features (b), (c) and (d) are present in both N-UNCD and clean diamond NEXAFS spectra (Gouzman *et al.*, 1999; Gruen *et al.*, 1996; Coffman *et al.*, 1996). The ratio of the sp^2/sp^3 -bonded carbon in N-UNCD thin film is an indication of the conductivity and grain size. The fraction of the sp^2 -bonded carbon is given by the following equation (Sumant *et al.*, 2007),

$$f_{sp^2} = \frac{I_{\text{sam}}^{\pi^*} I_{\text{ref}}(\Delta E)}{I_{\text{ref}}^{\pi^*} I_{\text{sam}}(\Delta E)}, \quad (1)$$

where $I_{\text{sam}}^{\pi^*}$ and $I_{\text{ref}}^{\pi^*}$ are the integrated areas for the carbon $1s-\pi^*$ peak from 284 eV to 286.8 eV in the N-UNCD and HOPG reference samples, respectively. $I_{\text{sam}}(\Delta E)$ and $I_{\text{ref}}(\Delta E)$ are areas calculated under the curves from 286.8 eV to 315 eV, which is contributed by the sp^3 -bonded carbon in the samples. The calculated sp^2 fraction for the tested N-UNCD film is 18.34%, corresponding to an average grain size of ~ 2.5 nm in the sampled region of the N-UNCD layer.

The NEXAFS structure was also observed in the detector current signal (data not shown). This effect arises from the details of the absorption length in the diamond near the incident contact (Muller *et al.*, 2014).

3.2. UNCD surface morphology

Prior research demonstrating the electrical characteristics of N-UNCD were conducted using films grown on nanoparticle seeded silicon or thin tungsten films (Bhattacharyya *et al.*, 2001). The conductivity was shown to be from the sp^2 carbon atoms accumulated along the grain boundaries. Small grain size (2–5 nm) assists in significantly reducing resistance by increasing the surface area to volume ratio, which explains the higher conductivity of UNCD compared with microcrystalline diamond films (Pradhan & Lin, 2009). Because our UNCD films were grown on unseeded single-crystal synthetic diamond, it is important to show that a similar nanocrystalline structure for high conductivity was obtained. Therefore, the N-UNCD contacts from UNCD I were characterized using an SEM (JOEL 7600F) with no coatings applied to the sample surface. Fig. 5(a) shows the morphology of the N-UNCD contacts on the diamond detector. Here, the grain size of the nanocrystalline structures is measured to be of the order of 5–15 nm and the size of the graphitic grain clusters is of the order of 45–90 nm, both of which are larger than that of the UNCD films grown on Si substrates.

The shape of the grains is determined by the gas components for growth (Jiang & Tzeng, 2011; Sankaran *et al.*, 2013). Specifically, the long and thin UNCD grains seen in Fig. 5(a) are attributed to the 20% nitrogen incorporation level with 1% CH_4 . This type of grain constitutes the uniform and smooth UNCD film surface. As shown in Fig. 5(b), there is a broken area on the surface during the UNCD film growth. The nucleation process can be observed from the independent spherical colonies which normally starts at the edges of the broken area. The aggregation process is triggered when the

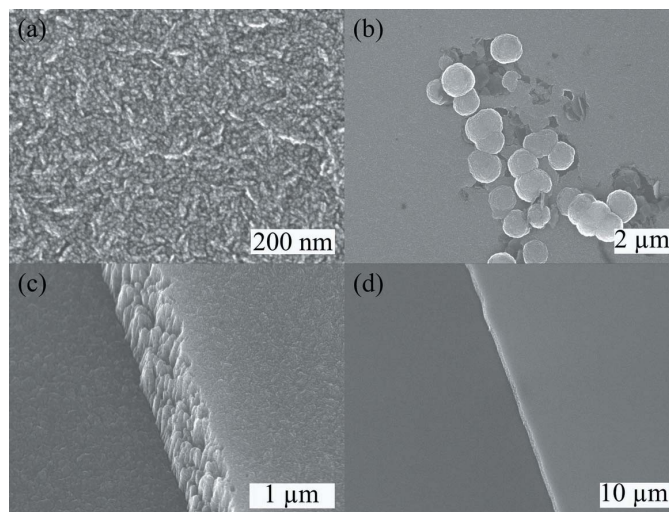


Figure 5 SEM images of the N-UNCD film from UNCD I illustrating (a) the nanocrystalline grain, (b) a smooth surface with spherical colonies from secondary nucleation, (c) microstructures of the sidewalls after RIE and (d) the profile of the etched sidewall.

surfaces of two spherical granules come into contact. This process corresponds to the nucleation mechanism of the nanocrystalline diamond film (Butler & Sumant, 2008).

The sidewall of the UNCD contacts after RIE with a Ni mask is illustrated in Figs. 5(c) and 5(d), indicating that the process results in a straight and clean sidewall profile. The resolution of the street size is high, with less than 1 μm error from the anisotropic etching rate. The presence of large granular crystallites at the edge (Fig. 5c) confirms the reduction of grain boundary areas, corresponding to the Raman spectrum results.

3.3. UNCD detector performance

The UNCD I detector, which simply functions as a quadrant-channel X-ray detector, was tested at CHESS first to confirm the feasibility of the UNCD contacts in detector performance. To determine the bias at which the current saturates (above which the detector has full charge collection), an $I-V$ curve was measured, see inset on Fig. 6(a). A $250 \mu\text{m} \times 200 \mu\text{m}$ monochromatic X-ray beam was used to illuminate the center of the UNCD I detector, signals were collected from the quadrant side using a Keithley electrometer (model 6517A) with a varied bias from -20 to 20 V applied to the single pad side. The signal increases rapidly with bias and achieves full collection at approximately 1.5 V. The corresponding electric field for saturation is calculated to be $0.028 \text{ V } \mu\text{m}^{-1}$, which is consistent with the values obtained previously for electronic-grade diamond detectors with Pt contacts. As the bias changes to the negative polarity, the $I-V$ curve behaves symmetrically to the positive polarity. The $I-V$ curves were also measured in several different positions on the UNCD I detector; similar saturation currents and full collection bias values confirmed the stability and uniformity of the N-UNCD contact performance.

Response calibration of the detector was performed under varied incident flux conditions, controlled by changing the thickness of an aluminium attenuator installed in front of the detector (part C, Fig. 2). The signals generated in the detector should have a linear relationship with the absorbed power which can be calculated from the incident photon flux and the photon energy (Bohon *et al.*, 2010). The intensity of the X-ray source was monitored by an ionization chamber. The incident flux can be then calculated by the source beam intensity and the transmission rates of the components along the path [CXRO database (Henke *et al.*, 1993)]. To achieve sufficient signal to detect under low-flux conditions, the beam size was expanded to 4 mm × 2 mm prior to response calibration by moving the slits (part A, Fig. 2). An operating bias of 10 V was applied to guarantee full collection during the measurements.

Results from the response calibration are shown in Fig. 6(a), illustrating the linearity between the absorbed power in the UNCD I detector and the corresponding current collected from the detector. The inverse slope of the fitted linear equation, calculated as 13.27 eV, represents the ionization energy of diamond, which is in agreement with the previously determined value of 13.3 eV as the electron–hole pair formation energy (Keister & Smedley, 2009). A standard deviation of 1% was observed in the ion chamber signal collection,

which explains the error for the response calibration (0.12 eV).

The same test was also performed on the UNCD III detector, with larger flux scale using the white X-ray beam in the XFP beamline at NSLS-II (Fig. 6b). When the incident flux is low, the current from the detector still follows the linear relationship with the absorption power. However, as the flux increases, the collected current starts to deviate from linearity. This can be explained by the resistivity through the contact, which was measured to be 0.81 Ω cm by a probe station (Signatone, 25 μm-tip), compared with the resistivity of 30 Ω cm from the conventional platinum contacts. When the current exceeds a certain value (it is 200 μA in the UNCD III detector), the resistivity of the UNCD contacts will lead to a bias drop between the wire-bonding foot and the center of contacts, making the local electric potential at the center far away from the grounding level. As a result, the local electric field will significantly decrease and is possible to be smaller than the electric field for saturation. At that point, the carriers generated in the diamond will not be fully collected and the UNCD detector will no longer function as a flux monitor. The relatively high resistivity (compared with the high-conductive metal contacts) limits the application of UNCD detectors as flux monitors in ultrahigh-flux X-ray beam.

Position calibration was conducted at CHESS with a 250 μm × 200 μm beam scanned horizontally (indicated as the X direction) or vertically (indicated as the Y direction) across the electrode gap area of the UNCD I detector. The position of the X-ray beam on the UNCD detector can be calculated by the current collected from four channels as

$$X = G_x \frac{(I_B + I_D) - (I_A + I_C)}{I_A + I_B + I_C + I_D}, \quad (2)$$

$$Y = G_y \frac{(I_A + I_B) - (I_C + I_D)}{I_A + I_B + I_C + I_D}. \quad (3)$$

In these equations, I_A , I_B , I_C and I_D represent the signals independently collected from four channels indicated in Fig. 1(a); G_x and G_y are sensitivity constants related to the beam size. In the measurements, the signals from the four channels and the detector positions were collected and recorded simultaneously. The normalized position calibration results are illustrated in Fig. 7. G_x and G_y can be calculated by the FWHM of the fitted Gaussian curves from the derivative position calibration curves, as shown in Fig. 7. By applying equations (2) and (3), the beam position can be determined. To evaluate the consistency between the actual beam position and the calculated results from the detector signals, the UNCD I detector was moved to several positions with the X-ray beam fixed, so that the accurate beam position could be obtained from the coordinates of the high-accuracy micromotor. The experimental results reveal that the deviations between the calculated beam positions and the actual motor positions are smaller than 0.5% in both directions.

From Fig. 7, deviation from linearity is observed when the detector was moved to the edge of the active area. This deviation may arise from the fluctuation of the unstable X-ray

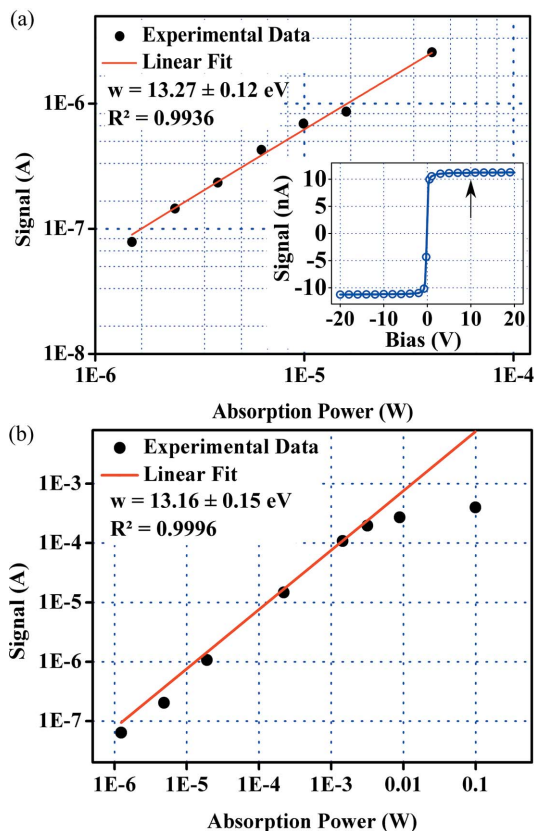


Figure 6
(a) Response calibration of the UNCD I detector, $W = 13.27 \text{ eV} \pm 0.12 \text{ eV}$. The inset is the I – V curve of the UNCD I detector and the arrow indicates the operating bias for the response calibration. (b) Response calibration of the UNCD III detector, $W = 13.16 \text{ eV} \pm 0.15 \text{ eV}$, with obvious deviation from linearity as flux becomes high.

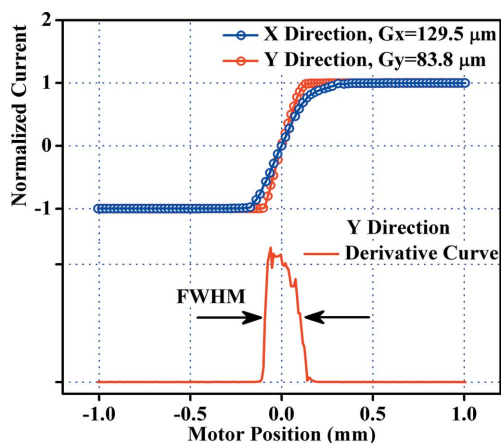


Figure 7
Position calibration curves in both X (horizontal) and Y (vertical) directions from the UNCD I detector and the corresponding derivative curve from the Y direction calibration.

beam itself. The beam drift was monitored overnight with the detector fixed in position with the nominally $250\ \mu\text{m} \times 200\ \mu\text{m}$ beam centered between all four pads. The standard deviation of the beam position was measured to be $4.60\ \mu\text{m}$ in the horizontal direction and $2.88\ \mu\text{m}$ in the vertical direction, which is within the resolution requirements of the G2 beamline. Furthermore, G_x and G_y can be used to evaluate the accurate size of the beam hitting the detector. In this test, the beam size was calculated to be $259.0\ \mu\text{m} \times 167.6\ \mu\text{m}$; the discrepancy from the beam dimensions set by the upstream slits is likely due to a combination of the beam divergence and the low accuracy of the slit motors.

X-ray beam-induced current response maps were collected with a $250\ \mu\text{m} \times 200\ \mu\text{m}$ incident X-ray beam at the G2 beamline (low-flux monochromatic X-rays), by moving the UNCD I detector through an area of $4\ \mu\text{m} \times 4\ \mu\text{m}$. The beam position was recorded as the coordinates of the micro-motor and signals produced at each position were collected, composing a mosaic response map to confirm the uniformity of the detector. The response maps were collected under a series of different bias conditions, with both positive and negative polarities; no hot spots were observed in any of the maps. A response map under full collection conditions is illustrated in Fig. 8(a), profiling the shape of the N-UNCD contacts. A similar test was also performed for the UNCD II detector at the XFP beamline (high-flux white beam) and the

response map is shown in Fig. 8(b), representing clear edges for each channel and no leakage between channels. The high response along the edges of the active area is attributed to the backscattering from the copper part on the circuit board.

4. Conclusion

Diamond X-ray detectors with N-UNCD contacts have achieved excellent electrical performance for X-ray flux measurement and position calibration, including low saturation bias, uniform response maps and no evidence of photoconductive gain. The contacts have significant advantages over traditional metal contacts due to a lack of extra absorption edges, less absorption in the soft X-ray range, and similar material properties to the underlying detector material. The contacts can be grown on unseeded electronic-grade CVD diamonds, lithographically patterned with a combination of standard techniques and reactive ion etching, and allow direct application of wire bonds. The results indicate that N-UNCD is feasible for use as a contact material for diamond X-ray detectors resulting in an all-diamond radiation monitor applicable to nearly all synchrotron techniques. Work to improve the conductivity to extend the linearity of N-UNCD to higher X-ray fluxes is still needed. N-UNCD contacts share many of the advantages as other carbon-based contacts; however, they are expected to have better chemical resistance and can easily support intrinsic diamond protective layers.

Acknowledgements

The authors wish to thank Ming Lu for assistance in fabrication, Fernando Camino for advice on SEM, and Donald Pinelli for assembly and wire-bonding work. The authors are grateful to the Instrumentation Division (BNL) for the design and fabrication of printed circuit boards. The authors would also like to thank all of the CHESS staff for their assistance at the beamlines and CFN staff for assistance in the clean room. Research carried out (in whole or in part) at Brookhaven National Laboratory, which is supported by the US Department of Energy, Office of Basic Energy Sciences, under Contract No. DE-SC0012704 (CFN), DE-AC02-98CH10886 (NSLS), DE-SC0012704 (NSLS-II) and Office of High Energy Physics Award DE-SC0015841 and at the Center for Nanoscale Materials, a US Department of Energy Office of Science User Facility, and supported by the US Department of Energy,

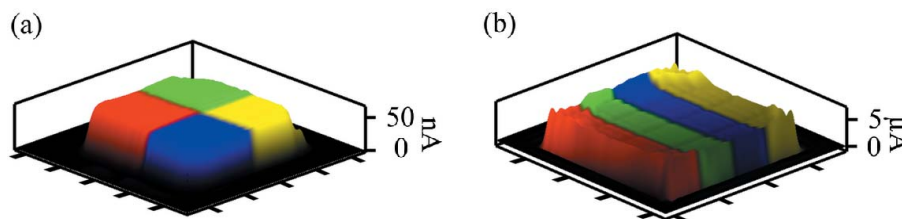


Figure 8
XBIC images of (a) UNCD I from low-flux monochromatic X-rays and (b) UNCD II from high-flux white beam, showing uniform response. The colors indicate the current from each of the four channels and each division represents 1 mm. The high response at the edges of UNCD II is from backscattering of the circuit board.

Office of Science, under Contract Nos. DE-AC02-06CH11357 and DE-SC0007482. The Case Center for Synchrotron Biosciences is supported by the National Institute of Biomedical Imaging and Bioengineering under P30-EB-009998. Use of CHESS is supported by the NSF and NIH/NIGMS via NSF award DMR-1332208.

References

- Arenal, R., Montagnac, G., Bruno, P. & Gruen, D. M. (2007). *Phys. Rev. B*, **76**, 245316.
- Bergonzo, P., Brambilla, A., Tromson, D., Marshall, R. D., Jany, C., Foulon, F., Gauthier, C., Solé, V. A., Rogalev, A. & Goulon, J. (1999). *J. Synchrotron Rad.* **6**, 1–5.
- Bhattacharyya, S., Auciello, O., Birrell, J., Carlisle, J. A., Curtiss, L. A., Goyette, A. N., Gruen, D. M., Krauss, A. R., Schlueter, J., Sumant, A. & Zapol, P. (2001). *Appl. Phys. Lett.* **79**, 1441–1443.
- Bohon, J., Smedley, J., Muller, E. & Keister, J. W. (2010). *Mater. Res. Soc. Symp. Proc.* **1203**, 239–244.
- Butler, J. E. & Sumant, A. V. (2008). *Chem. Vap. Deposition*, **14**, 145–160.
- Coffman, F. L., Cao, R., Pianetta, P. A., Kapoor, S., Kelly, M. & Terminello, L. J. (1996). *Appl. Phys. Lett.* **69**, 568–570.
- De Feudis, M., Caricato, A., Taurino, A., Ossi, P., Castiglioni, C., Brambilla, L., Maruccio, G., Monteduro, A., Broitman, E., Chiodini, G. & Martino, M. (2017). *Diamond Relat. Mater.* **75**, 25–33.
- Desjardins, K., Bordessoule, M. & Pomorski, M. (2018). *J. Synchrotron Rad.* **25**, 399–406.
- Garrett, D. J., Ganesan, K., Stacey, A., Fox, K., Meffin, H. & Prawer, S. (2012). *J. Neural Eng.* **9**, 016002.
- Gouzman, I., Shima-Edelstein, R., Comtet, G., Hellner, L., Dujardin, G., Roter, S. & Hoffman, A. (1999). *Diamond Relat. Mater.* **8**, 132–138.
- Gruen, D. M. (1999). *Annu. Rev. Mater. Sci.* **29**, 211–259.
- Gruen, D. M., Krauss, A. R., Zuiker, C. D., Csencsits, R., Terminello, L. J., Carlisle, J. A., Jimenez, I., Sutherland, D. G. J., Shuh, D. K., Tong, W. & Himpsel, F. J. (1996). *Appl. Phys. Lett.* **68**, 1640–1642.
- Henke, B., Gullikson, E. & Davis, J. (1993). *At. Data Nucl. Data Tables*, **54**, 181–342.
- Jiang, J.-H. & Tzeng, Y. (2011). *AIP Adv.* **1**, 042117.
- Keister, J. W. & Smedley, J. (2009). *Nucl. Instrum. Methods Phys. Res. A*, **606**, 774–779.
- Kuzmany, H., Pfeiffer, R., Salk, N. & Günther, B. (2004). *Carbon*, **42**, 911–917.
- Lohstroh, A., Sellin, P. J., Wang, S. G., Davies, A. W., Parkin, J., Martin, R. W. & Edwards, P. R. (2007). *Appl. Phys. Lett.* **90**, 102111.
- Muller, E. M., Gaowei, M., Ben-Zvi, I., Dimitrov, D. A. & Smedley, J. (2014). *Appl. Phys. Lett.* **104**, 093515.
- Muller, E. M., Smedley, J., Bohon, J., Yang, X., Gaowei, M., Skinner, J., De Geronimo, G., Sullivan, M., Allaire, M., Keister, J. W., Berman, L. & Héroux, A. (2012). *J. Synchrotron Rad.* **19**, 381–387.
- Muller, E. M., Smedley, J., Raghothamachar, B., Gaowei, M., Keister, J. W., Ben-Zvi, I., Dudley, M. & Wu, Q. (2009). *Mater. Res. Soc. Symp. Proc.* **1203**, 1203-J17-19.
- Narayan, R. (2013). *Diamond-Based Materials for Biomedical Applications*. Oxford: Woodhead Publishing.
- Pradhan, D. & Lin, I. N. (2009). *Appl. Mater. Interfaces*, **1**, 1444–1450.
- Ravel, B., Attenkofer, K., Bohon, J., Muller, E. & Smedley, J. (2013). *Rev. Sci. Instrum.* **84**, 103106.
- Ravel, B. & Newville, M. (2005). *J. Synchrotron Rad.* **12**, 537–541.
- Sankaran, K., Kumar, N., Dash, S., Chen, H., Tyagi, A., Tai, N. & Lin, I. (2013). *Surf. Coat. Technol.* **232**, 75–87.
- Sumant, A. V., Gilbert, P., Grierson, D. S., Konicek, A. R., Abrecht, M., Butler, J. E., Feygelson, T., Rotter, S. S. & Carpick, R. W. (2007). *Diamond Relat. Mater.* **16**, 718–724.
- Yuan, W., Fang, L. P., Feng, Z., Chen, Z. X., Wen, J. W., Xiong, Y. & Wang, B. (2016). *J. Mater. Chem. C*, **4**, 4778–4785.
- Zhou, T., Ding, W., Gaowei, M., De Geronimo, G., Bohon, J., Smedley, J. & Muller, E. (2015). *J. Synchrotron Rad.* **22**, 1396–1402.